I&EC research
Industrial & Engineering Chemistry Research

pubs.acs.org/IECR
Article

On Comparing Packed Beds and Monoliths for CO_2 Capture from Air Through Experiments, Theory, and Modeling

Valentina Stampi-Bombelli, Alba Storione, Quirin Grossmann, and Marco Mazzotti*

Cite This: *Ind. Eng. Chem. Res.* 2024, 63, 11637−11653

ABSTRACT: This study compares the performance of amine-functionalized γ-alumina sorbents in the form of 3 mm γ-alumina pellets and of a γ-alumina wash-coated monolith for CO_2 capture for direct air capture (DAC). Breakthrough experiments were conducted on the two contactors to analyze the adsorption kinetics and performance for different gas feeds. A constant pattern analysis revealed dominant mass transfer resistances in the gas film and in the pores, with axial dispersion also observed, particularly at higher concentrations. A 1D, physical model was used to fit the experiments and thus to estimate mass transfer and axial dispersion coefficients, which appear to be consistent with the hypotheses derived from constant pattern analysis. A dual kinetic model to describe mass transfer was found to better describe the tail behavior in the monolith, whereas a pseudo-first-order model was sufficient to describe breakthroughs on packed beds. A substantial two-order magnitude decrease in mass transfer coefficients was noted when reducing the feed concentration from 5.6% to 400 ppm CO_2, thus underscoring the significant mass transfer limitations observed in DAC. Comparison between the contactors revealed notably higher mass transfer coefficients in the monolith compared to the packed beds, which are attributed to shorter diffusion lengths and lower equilibrium capacity. While the faster mass transfer coefficients observed in the monolith experiments led to reduced specific energy consumption and increased adsorption productivity compared to the packed bed at 400 ppm, no significant improvement was observed for the same process at the higher concentration of 5.6% CO_2 in the feed. This finding highlights the need to tailor the contactor design to the specific gas separation requirements. This research contributes to the understanding and quantification of mass transfer kinetics at DAC concentrations in both packed bed and monolith contactors. It demonstrates the crucial role of the contactor in DAC systems and the importance of optimizing the adsorption step to enhance productivity and DAC performance.

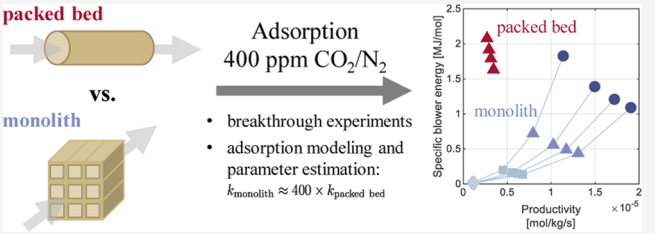

1. INTRODUCTION

Humankind is on a path to likely overdraw the carbon budget associated with the 2 °C target established by the Paris Agreement in 2015.[1] In addition to exploiting conventional mitigation and adaptation options (i.e., measures to reduce emissions of greenhouse gases and to cope with the changing climate, respectively), humankind will have to deploy technologies to counteract climate change. In particular, negative emission technologies (NETs) can rewind the carbon budget by permanently removing CO_2 from the atmosphere. NETs will also be needed to compensate for unavoidable emissions (aviation, chemicals, agriculture) in a net-zero−CO_2−emissions world, where average temperatures are stabilized. Direct capture of CO_2 from ambient air [*direct air capture*, (DAC)] coupled with permanent CO_2 storage is a key component of NETs.[2] DAC can be realized through different approaches, two of which are rather established (other methods, for instance, based on electrochemistry are at an earlier stage of development): absorption in alkaline aqueous solutions or adsorption on suitable solid sorbents. Between the two methods, the latter offers distinct advantages, including the potential for lower energy consumption, modularity, and reduced environmental impact associated with solvent use and disposal.[3−5]

Extensive scientific research has emphasized the importance of the development and optimization of sorbent materials for adsorption-based DAC.[6] The quest for suitable sorbents has driven investigations into materials with high CO_2 selectivity over N_2 and O_2, high CO_2 capacity at the relevant low concentrations, long lifetime, and stable and favorable adsorption properties in the presence of water, given the inevitable humidity of the air. The literature showcases the significant progress made in sorbent development, including the exploration of amine-functionalized materials on multiple supports such as oxides[7−12] and metal−organic frameworks.[13,14] Other than having high uptake capacity at low concentrations of CO_2, such amine-functionalized materials exhibit two advantages, namely the enhanced CO_2 adsorption capacity in the

Received: April 11, 2024
Revised: May 30, 2024
Accepted: May 30, 2024
Published: June 18, 2024

presence of water[15] and the low temperature requirements for sorbent regeneration.[5]

While sorbent development has been one of the primary research focuses, other important requirements of DAC systems have also been recognized. Once such challenge is posed by the dilute concentration of CO_2 in the air, which necessitates the processing of large volumes of air to capture a meaningful amount of CO_2. To provide perspective, capturing 1 kg of CO_2 requires processing approximately 1400 m^3 of air under standard laboratory conditions. Consequently, capturing CO_2 from air in a practical manner requires handling large volumetric flows and, as a result, high velocities. To decrease the electrical energy consumption of the fan blowing large volumes of air through the contactor, novel contactor configurations with low pressure drops are being analyzed for sorbent-based DAC applications. Among these contactors, monolith structures have gained attention due to their wide use as low pressure drop catalyst supports, particularly in the automotive industry. These structures offer high porosity and have been shown in point-source capture studies to enhance mass transfer kinetics.[16−18] Additionally, efforts have been made to increase porosities in packed bed geometries, resulting in thin packed bed configurations that reduce pressure drops.[19,20] Both approaches have been considered both in industrial development, as evidenced by patent applications,[19,21,22] and in the academic literature related to DAC.[4,15,23−31]

In DAC literature, various technical,[15,23−25] techno-economic,[4,26−30] and life cycle assessment studies[31] have been performed both on sorbents in pellet form arranged in various packed bed configurations[15,24,25,28−30] and on sorbents in monolith form.[23,26−29] Within the DAC modeling works, CO_2 equilibrium data have played a pivotal role in informing cycle, energy, and cost calculations. Notably, of the aforementioned studies, only two acquired mass transfer kinetic data from breakthrough experiments,[15,24] while others either resorted to correlations[26] or relied on assumptions, supplementing their analyses with sensitivity studies on the effect of changing mass transfer coefficients.[4,25] The results of sensitivity analyses underscored the significant impact of mass transfer coefficients on DAC performance, to the point that an inaccurate estimation of the mass transfer coefficient could severely affect the conclusions and result in major differences in specific energy requirement and productivity.[4] These findings were reinforced by a comprehensive study,[32] which identified the overall mass transfer coefficient as one of the most influential parameters affecting specific energy consumption, productivity, and purity among 15 key parameters analyzed within a DAC adsorption cycle. These observations highlighted the critical importance of accurately modeling mass transfer kinetics within the DAC framework but also highlighted the lack of characterized kinetic data in DAC literature. Despite the availability of experimental kinetic data in DAC concentrations for both pellets[13,33,34] and monoliths,[35−38] only two studies have undertaken the task of quantifying this data with kinetic models,[34,38] while most of the papers put a greater emphasis on sorbent synthesis rather than on characterizing kinetics. Indeed, while notable observations regarding irregular breakthrough profiles[35] and slow kinetics[7,13,33] have been made, the observed mass transfer dynamics have lacked the quantitative characterization necessary for accurate adsorption modeling, thus hindering the development of strategies to address the observed kinetic limitations.

Therefore, we acknowledge the disparity between the necessity for detailed kinetic data at DAC concentrations, on which to base process calculations, and its availability in the current literature. With this work, we aim to bridge this gap by presenting experiments performed at DAC concentrations and analyzing them both qualitatively and quantitatively. Given the significance of both the packed bed and monolith geometries in DAC applications, we investigated both types of contactors. Breakthrough experiments were performed under conditions allowing for the full development of the mass transfer zone, thus enabling an accurate characterization of the adsorption kinetics using a 1D model. To achieve this, the following steps were undertaken.

- breakthrough experiments were conducted to study the adsorption kinetics under dry conditions on a packed bed of amine-functionalized γ-alumina pellets and on an amine-functionalized γ-alumina wash-coated monolith, at different feed velocities and concentrations;
- with a simple methodology derived from a constant pattern analysis, the fundamental mechanisms controlling adsorption were qualitatively evaluated by examining the effects of varying operating conditions on the breakthrough profiles;
- a one-dimensional physical model, considering both a conventional pseudo-first-order (PFO) kinetic model and a dual kinetic (DK) model to describe mass transfer on amine sorbents, was utilized to fit dispersion data, to validate literature mass transfer correlations, and to confirm the findings from the constant pattern solution;
- last, the adsorption performance of the contactors was compared, contextualizing their characterization within DAC-relevant circumstances.

2. METHODOLOGY

In this section, we describe the materials used in this study, along with the experimental setup and experimental campaign performed. Subsequently, we introduce the adsorption model utilized for quantitatively estimating transport parameters from the breakthrough experiments while comparing two models to describe adsorption kinetics. We then outline a methodology derived from the constant pattern solution, used for the identification of limiting adsorption mechanisms from breakthrough curves. Finally, we define the key performance indicators that allow a comparison of the two contactors studied in the range of experimental conditions considered in this work.

2.1. Materials. In this study, we examined two distinct sorbent geometries. Specifically, we have investigated mesoporous γ-alumina pellets in the shape of 3 mm hollow rings, which are commercially available materials provided by the company Saint Gobain, and a γ-alumina-coated mullite honeycomb monolith, which is an adaptation of a commercial material provided by the company HUG Engineering. The γ-alumina wash-coat applied by HUG Engineering resulted in the creation of mesoporous pockets of γ-alumina throughout the macropores of the mullite support, as illustrated in Figure 1. The γ-alumina of both contactors was functionalized with triamine via a water-aided amine grafting protocol that has been described elsewhere.[36] Pure-component CO_2 adsorption isotherms of the pellets were measured at 25, 50, and 90 °C by using a Microtrac BELSORP Max volumetric device. The CO_2 adsorption data at 25 °C is displayed in Figure S1, along with that for N_2, which was obtained using the same procedure

https://doi.org/10.1021/acs.iecr.4c01392
Ind. Eng. Chem. Res. 2024, 63, 11637−11653

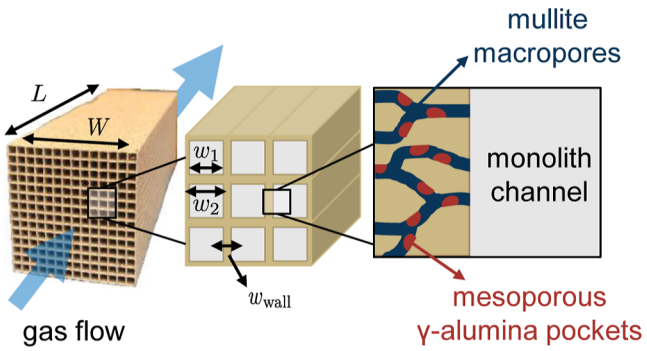

Figure 1. Visual representation of the γ-alumina-coated mullite monolith provided by HUG Engineering, with 12 × 12 channels and walls with a macroporous structure given by the mullite and the mesoporous structure given by the γ-alumina pockets.

and which demonstrates no N_2 adsorption. The sets of data at the three temperatures were used to compute the isosteric heat of adsorption of CO_2 using the Clausius−Clapeyron equation, and the following temperature-dependent Toth equation was used to describe the adsorption isotherms of CO_2 on amine-functionalized γ-alumina using eqs 1−4. The fitted parameters of the Toth isotherm are reported in Table 1. For modeling

Table 1. Toth Isotherm Parameters Fitted to the CO_2 Adsorption Data on the Amine-Functionalized γ-Alumina Pellets at 298 K Reported in the Work by Grossmann et al.[36]

	units	value
T_0	[K]	298
n_{s0}	[mol kg^{-1}]	1.23
b_0	[kPa^{-1}]	4839
t_0	[-]	0.25
ΔH_0	[kJ mol^{-1}]	70
χ	[-]	0
α	[-]	0.11

purposes, the isotherm of the monolith was calculated as $q^*_{mono} = 0.035\, q^*_{pellet}$, as the CO_2 uptake per total monolith mass was 3.5% of that of the pellets. Detailed properties of the mesoporous γ-alumina pellets and the γ-alumina-coated mullite honeycomb monolith are reported in Tables 2 and 3, respectively.

$$q_{pellet}(p_{CO_2}, T) = \frac{n_s(T) b(T) p_{CO_2}}{(1 + (b(T) p_{CO_2})^{t(T)})^{1/t(T)}} \quad (1)$$

$$n_s(T) = n_{s0} \exp\left(\chi\left(1 - \frac{T}{T_0}\right)\right) \quad (2)$$

$$b(T) = b_0 \exp\left(\frac{\Delta H_0}{R T_0}\left(\frac{T_0}{T} - 1\right)\right) \quad (3)$$

$$t(T) = t_0 + \alpha\left(1 - \frac{T_0}{T}\right) \quad (4)$$

2.2. Experimental Setup. The schematic of the breakthrough apparatus used in this study is shown in Figure 2. The setup comprised a feeding system, a contactor consisting of either a packed bed or a monolith, and a gas analysis section. To facilitate dead volume measurements, a thin gas line of negligible volume bypassing the column was installed. The feeding system

Table 2. Properties of the Commercial Saint-Gobain γ-Alumina Pellets and the Packed Bed Considered in This Work

	units	value	ref
material properties			
material	[-]	γ-alumina	a
shape	[-]	rings	a
pellet size, d_p	[mm]	3	a
pore size	[nm]	13.3	a
pore volume	[cm^3 g^{-1}]	0.68	a
material density, ρ_s	[kg m^{-3}]	3600	b
pellet density, ρ_p	[kg m^{-3}]	1044	c
pellet porosity, ε_p	[-]	0.71	c
specific heat capacity	[J kg^{-1} K]	784	b
contactor properties			
length, L	[cm]	32.5	
diameter	[cm]	3.37	
weight (regenerated)	[g]	187	

[a]Saint-Gobain. [b]NIST database. [c]Determined from the pellet size, material density, and pore volume.

Table 3. Properties of the Commercial HUG Engineering γ-Alumina-Coated Monolith Considered in This Work

	units	value	ref
material properties			
material	[-]	6.9 wt.% γ-alumina on mullite	a
length, L	[cm]	13	b
width, W	[cm]	2.9	b
weight (regenerated)	[g]	57.82	b
wall thickness, w_{wall}	[mm]	0.4	b
channel thickness, w_1	[mm]	2	b
mullite pore size	[μm]	15−20	a
γ-alumina pore size	[nm]	28	b
CPSI	[-]	∼100	a
wall porosity, ε_p	[-]	0.48	a
monolith porosity, ε	[-]	0.68	b
total number of cells, N	[-]	144	b
contactor properties			
length	[cm]	15	
width	[cm]	3.2	

[a]HUG engineering. [b]Measurement or calculation.

was equipped with two Bronkhorst mass flow controllers (MFC), capable of operating at high or low flow rates (MFC 1: 0−250 nmL/min, MFC 2: 0−25 nL/min). The inlet pressure and temperature were monitored by using probes placed at the column inlet. The outlet of the column was equipped with two flow-through CO_2 sensors (open to the atmosphere), namely Vaisala GMP343 and Vaisala GMP251, capable of measuring CO_2 concentrations in the range from 0 to 2000 ppm and from 0 to 20%, respectively.

The contactor used for the pellet experiments consisted of a cylindrical packed bed column 3.37 cm in diameter and 32.5 cm in length, L, containing 187 g of the amine-functionalized γ-alumina pellets. The column was equipped with heating wires surrounding its external wall and a thermocouple positioned at the center of the column ($z = 0.5\, L$) to measure the temperature of the pellets. The contactor used for the monolith experiments consisted of a column with a square cross-section of 3.2 × 3.2 cm^2 and a length, L, of 15 cm, which accommodated a single monolith. A textile felt was placed between the monolith and the

https://doi.org/10.1021/acs.iecr.4c01392
Ind. Eng. Chem. Res. 2024, 63, 11637−11653

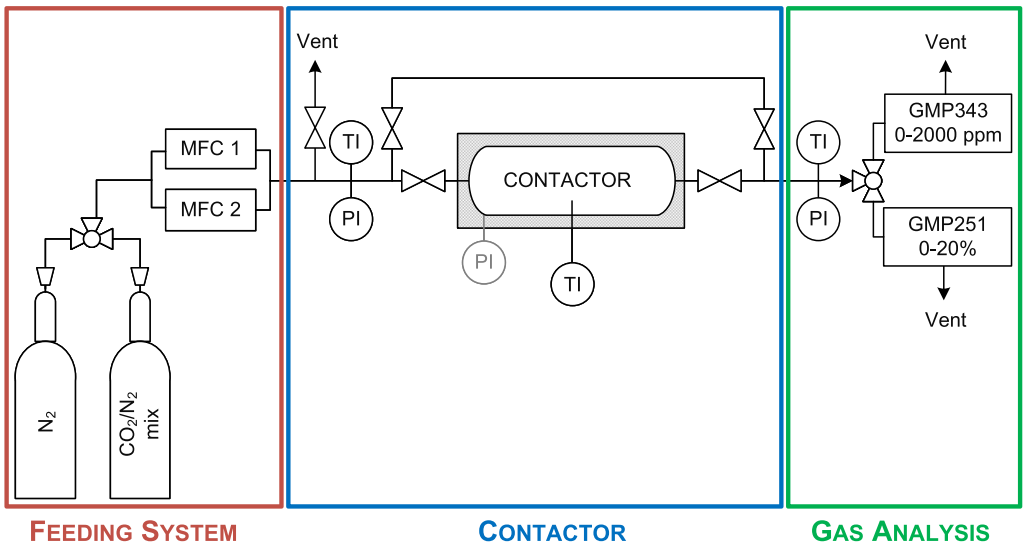

Figure 2. Flow sheet of the experimental fixed-bed setup, made up of a feeding system, an interchangeable column that can accommodate the cylindrical pellet packed bed and the monolith column, and a gas analysis section. Abbreviations used: MFC, mass flow controller; TI, thermocouple; PI, pressure indicator; GMP343, Vaisala CO_2 sensor in the range of 0−2000 ppm; GMP251, Vaisala CO_2 sensor in the range of 0−20%.

Table 4. Momentum Balance, Mass Transfer Correlations, and Axial Dispersion Correlations Used for the One Dimensional Adsorption Model Described in Section 2.4[a]

	pellets	monolith
momentum balance		
	$\frac{\partial p}{\partial z} = 150\frac{\mu(1-\varepsilon)^2}{\varepsilon^3 d_p^2}u_s + 1.75\frac{\rho(1-\varepsilon)}{\varepsilon^3 d_p}\lvert u_s\rvert u_s$ (16)	$\frac{\partial p}{\partial z} = \frac{32\mu}{w_1^2}u$ (17)
mass transfer correlations		
film coefficient[16]	$k_f = \frac{3}{r_p}k_f'$ with $k_f' = \frac{D_m}{d_p}Sh$ (18) and $Sh = 2 + 1.1\,Re^{0.6}Sc^{0.33}$ (20)	$k_f = \frac{4w_1}{w_2^2 - w_1^2}k_f'$ with $k_f' = \frac{D_m}{w_1}Sh$ (19) and $Sh = 2.696\left(1 + 0.139\left(\frac{w_1}{L}\right)ReSc\right)^{0.81}$ (21)
pore coefficient[16,50]	$k_p = \frac{15\varepsilon_p D_p}{r_p^2}$ (22)	$\frac{1}{k_p} = \frac{1}{k_{p,\text{mullite}}} + \frac{1}{k_{p,\text{al}}}$ with $k_{p,\text{al}} = \frac{15\varepsilon_{\text{al}}D_{\text{al}}}{r_{\text{al}}^2}$ (23) and $k_{p,\text{mullite}} = \frac{24D_{\text{mullite}}r_1}{(r_2 - r_1)^2(5r_2 + 3r_1)}$ (24)
solid coefficient	$k_s = \frac{15D_s}{r_c^2}$ (25)	$k_s = \frac{15D_s}{r_c^2}$ (26)
axial dispersion correlations[16,51]		
	$D_L = ud_p\left(\frac{0.45 + 0.55\varepsilon}{ReSc} + 0.5\right)$ (27)	$D_L = D_m + \frac{u^2 w_1^2}{192D_m}$ (28)

[a] $D_p = D_K/\tau_{\text{al}}$ and $D_{\text{al}} = D_K/\tau_{\text{al}}$, with $D_K = d_{\text{pore}}\sqrt{8RT/(\pi M)}/3$ and $\tau_{\text{al}} = 2.5$; $D_{\text{mullite}} = D_m/\tau_{\text{mullite}}$, with $\tau_{\text{mullite}} = 2$.

internal column wall at the inlet and outlet in order to keep the monolith in place. A heating−cooling jacket surrounded the contactor, and the monolith temperature was measured with a thermocouple positioned at the end of the monolith ($z = L$). At the inlet, the monolith column was equipped with a conical flange and a gas distributor that allowed for the gas to distribute evenly through the whole cross section of the monolith. A pressure sensor was placed in the inlet conical section to accurately measure the pressure.

2.3. Experimental Campaign. *2.3.1. Regeneration Experiments.* Prior to each breakthrough experiment, the contactors were regenerated by heating the sorbents to 100 °C and purging them with N_2 at 1 mmol s^{-1} on the packed bed and 0.5 mmol s^{-1} on the monolith. Given that the primary focus of the study was the analysis of the adsorption step, the N_2 purge was utilized solely for the purpose of characterizing the CO_2 desorption from the column rather than to replicate the conditions used in a full adsorption cycle. Regeneration was set to last 3 h on the monolith (30 min ramp +2.5 h at 100 °C) and to last 4 h on the packed bed (30 min ramp +3.5 h at 100 °C). In both cases, this time was sufficient for the CO_2 outlet concentration to reach zero. At the end of regeneration, the contactor was cooled and closed.

2.3.2. Breakthrough Experiments. Once the contactors cooled to adsorption temperature, breakthrough experiments were performed. The adsorption temperature was dictated by

https://doi.org/10.1021/acs.iecr.4c01392
Ind. Eng. Chem. Res. 2024, 63, 11637−11653

the lab temperature because of the absence of active cooling in the packed bed column, thus resulting in an adsorption temperature of 22 °C for the monolith and ∼ 24 °C for the packed bed. Considering the rather small variation of the CO_2 isotherm within this 2 °C range, we conclude that the impact of the temperature difference on the experiments is negligible. The breakthrough experiments were carried out until the outlet CO_2 concentration reached at least 90% of the feed concentration. For each feed velocity examined, the dead volume time, representing the delay in the CO_2 signal caused by the dead volumes surrounding the contactor, was determined by flowing the gas through the bypass and subtracting that time from the breakthrough experiments. In all cases, the dead volume time was negligible with respect to the total breakthrough duration.

2.4. Modeling Adsorption. *2.4.1. Model Equations.* The adsorption model used is a first principles model of a transient, one-dimensional cylindrical column as described in previous works.[24,39] For the sake of brevity, the material and energy balances of the model used are not presented in this work, and can be found in eqs 1−6 of the work by Casas et al.[39] The following assumptions are made.

- the model is one-dimensional in the axial direction, with no radial gradient in temperature, concentration, or velocity;
- the fluid is an ideal gas and is described accordingly;
- the solid and gas phases are in thermal equilibrium;
- the heat capacities, the viscosity, the isosteric heat of adsorption and the heat transfer coefficients are constant;
- the momentum balance is not transient and it is assumed that the pressure drop reaches steady state conditions instantaneously.

The model was adapted to also describe adsorption in monolith contactors. The monolith contactor's square channel was modeled as a cylindrical channel with the same cross section to ensure the same gas velocity. Additionally, the Ergun equation used for describing the momentum balance in the packed bed was replaced by the Hagen-Poiseuille equation (eqs 16 and 17 in Table 4). Axial dispersion coefficients were characterized as polynomial functions that depend on the gas velocity according to eqs 5 or 6 for the packed bed and the monolith, respectively

$$D_{L,\text{pellets}} = p_1 u + p_2 \tag{5}$$

$$D_{L,\text{monolith}} = p_1 u^2 + p_2 \tag{6}$$

2.4.2. Mass Transfer Models. Adsorption on amine-functionalized sorbents often exhibits asymmetric CO_2 breakthrough profiles, characterized by a sharp breakthrough and a prolonged tail while approaching saturation.[40−43] Bollini et al. hypothesized that this arises from the heterogeneous nature of the aminopolymer layer formed during grafting, which results in more and less accessible amine sites, each with distinct saturation capacities and rates of mass transfer.[41,42] Given that water-aided amine grafting is known to induce amine polymerization,[44,45] it is reasonable to assume a heterogeneous nature of the amine adsorption sites. The long tail in the breakthrough is thus associated with a slower rate of mass transfer within the amine layer compared with the rate of mass transfer to the surface amine sites. Conventional models may fail to accurately capture the asymmetry of the breakthrough curve, which prompted the opportunity to develop dual kinetic models instead.[40,42,43] In this work, we investigated both the conventional pseudo-first-order (PFO) model and the dual kinetic (DK) model proposed by Kalyanaraman et al.[43] and compare their capability and accuracy in describing the experimental results. These two models are summarized shortly below.

- The pseudo-first-order model is a linear driving force (LDF) model with the limiting mass transfer resistance in the solid phase; k is the overall mass transfer coefficient:

$$\frac{\partial q}{\partial t} = k(q^* - q) \tag{7}$$

- The dual kinetic model assumes two types of adsorption sites, namely the easily accessible *surface* amine sites and the *bulk* amine-layer sites, with adsorbed phase concentrations q_1 and q_2, respectively, and:[43]

$$q = q_1 + q_2 \tag{8}$$

Two material balances are formulated for the surface and for the bulk adsorption sites, each with its specific mass transfer coefficient, k_1 and k_2[43]

$$\frac{\partial q_1}{\partial t} = k_1(\eta q^* - q_1) \tag{9}$$

$$\frac{\partial q_2}{\partial t} = k_2((1-\eta)q^* - q_2) \tag{10}$$

The parameter η is the fraction of surface sites, hence ηq^* is their equilibrium loading capacity; $(1-\eta)$ is the fraction of bulk sites and $(1-\eta)q^*$ is their equilibrium loading capacity.

2.4.3. Mass Transfer Coefficient Determination. The overall mass transfer coefficient for the PFO model was computed considering three resistances in series, namely in the gas film, in the gas pore and in the solid, with mass transfer coefficients k_f, k_p and k_s, respectively[46−49]

$$\frac{1}{k} = \frac{1}{k_f}\frac{q^*_{p,\text{in}}}{c_{\text{in}}} + \frac{1}{k_p}\frac{q^*_{p,\text{in}}}{c_{\text{in}}} + \frac{1}{k_s} \tag{11}$$

Kalyanaraman et al. proposed that the resistance to reach the surface amine sites in the DK model includes the resistance in the gas film, in the gas pore and in the surface amine layer,[43] similarly to k in the PFO model. The overall resistance to reach the bulk amine-layer sites consists of these same resistances in series, plus the transport resistance within the bulk amine layer.[43] Thus, we define k_1 and k_2 as follows

$$\frac{1}{k_1} = \frac{1}{k_f}\frac{q^*_{p,\text{in}}}{c_{\text{in}}} + \frac{1}{k_p}\frac{q^*_{p,\text{in}}}{c_{\text{in}}} + \frac{1}{k_s} \tag{12}$$

$$\frac{1}{k_2} = \frac{1}{k_1} + \frac{1}{k_{s,\text{amine}}} \tag{13}$$

When the impact of a variation in velocity on the overall mass transfer coefficient is small, the film mass transfer coefficient and the pore mass transfer coefficient can be combined into one parameter, called k_g, which accounts for the overall mass transfer resistance in the gas phase. In this case, the overall mass transfer coefficient can be written as

$$\frac{1}{k_1} = \frac{1}{k_g}\frac{q^*_{p,\text{in}}}{c_{\text{in}}} + \frac{1}{k_s} \tag{14}$$

https://doi.org/10.1021/acs.iecr.4c01392
Ind. Eng. Chem. Res. 2024, 63, 11637−11653

$$\frac{1}{k_g} = \frac{1}{k_f} + \frac{1}{k_p} \tag{15}$$

2.4.4. Parameter Estimation Using Literature Correlations. Literature correlations to estimate axial dispersion and mass transfer coefficients (p_1, p_2, k_f, k_p, and k_s) in the packed bed and in the monolith are summarized in Table 4. In order to account for the bimodal structure of the monolith pores, comprising the macropores of the mullite support and the mesopores of the γ-alumina pockets, the mass transfer coefficient in the gas pores, denoted as k_p, was modeled as determined by the resistances of these two phases in series. The pore mass transfer coefficient in the mullite macropores, called $k_{p,\text{mullite}}$, was calculated using established correlations from the literature, as in eq 24.[50] The mass transfer coefficient in the γ-alumina pockets, $k_{p,\text{al}}$, was defined assuming spherical γ-alumina pockets of radius r_{al} and using Glueckauf's expression for the pore mass transfer coefficient,[52] as in eq 23. A sensitivity analysis on all of the realistic values of the size of the γ-alumina pockets, r_{al}, showed that the mass transfer resistance in these pockets was negligible with respect to that in the mullite macropores, therefore resulting in $k_p = k_{p,\text{mullite}}$.

2.4.5. Parameter Estimation from the Experiments. In the following, we outline the methodology employed for estimating transport parameters from the breakthrough experiments. Given that the active sorbent for both contactors is triamine-grafted γ-alumina, we tested the hypothesis that the fraction of easily accessible surface amine sites (η) and that the mass transfer coefficients in the amine (k_s and $k_{s,\text{amine}}$) are constant in both contactors and for all experiments. Therefore, in order to be consistent with the physical picture of the adsorbent and of the mass transfer resistances given above, we carried out the parameter estimation exercise by.

- Keeping η, k_s, and $k_{s,\text{amine}}$ constant for all experiments;
- Letting the axial dispersion coefficient, D_L, vary with gas velocity according to eqs 5 and 6, whereby the parameters p_1 and p_2 are the same for experiments in the same contactor but different between contactors;
- Letting both k_1 and k_2 vary for the different contactors and the different operating conditions according to eqs 12 and 13, while analyzing and discussing changes in k_f at different velocities and keeping the mass transfer coefficient in the pore, k_p, constant for the experiments in the same contactor (but different between contactors).

2.4.5.1. PFO Model. Using the PFO model, estimation of k and D_L from the breakthrough experiments was carried out by minimizing over θ_1 and θ_2 the maximum likelihood estimate (MLE), defined as

$$\Phi(\theta_1, \theta_2) = \sum_{i=1}^{N_v} \ln\left(\sum_{j=1}^{N_p} \left(\frac{y_{ij} - \hat{y}_{ij}(\theta_1, \theta_2)}{\underline{y}_{ij}^{\max}} \right)^2 \right) \tag{29}$$

where N_v and N_p are the number of variables and the number of observations, respectively. The observed variables were the mole fractions at the exit of the column. The symbol $\underline{y}_{ij}^{\max}$ is the maximum value of $\underline{y}$, while the hat symbol denotes the estimated model outputs. The objective function Φ was minimized using the Matlab "fminsearchbnd" routine.[53] Then, constant sets of k_f, k_p, p_1, and p_2 for each contactor were fitted eqs 5,6 and 11 using the estimated values of k and D_L.

2.4.5.2. Dual Kinetic Model. The DK model was fitted to the breakthrough curves to estimate k_1, k_2, η, and D_L in each experiment. Various combinations of these parameters were found to effectively capture the breakthrough profiles. Based on the contributions detailed in eq 12, k_1 represents the mass transport that is responsible for the initial part of the breakthrough curve. Additionally, D_L influences only the initial part of the slope and not the elongated tails. Consequently, to restrict the feasible space of solutions under these physical constraints, estimation of the four parameters was divided in two steps. Initially, k_1 and D_L were estimated by minimizing the MLE in the initial part of the breakthrough curve (up to 70% of the uptake). Then, η and k_2 were estimated by considering the entire breakthrough profile through a sensitivity analysis on these parameters. Finally, constant sets of k_f, k_p, p_1, and p_2 for each contactor, along with constant k_s and $k_{s,\text{amine}}$ for both contactors, were determined using the estimated values of k_1, k_2, η, and D_L, and eqs 5,6 12, and 13.

2.4.5.3. Heat Transfer Coefficients. The value of the convective heat transfer coefficient from the external surface of the contactor wall to the ambient environment, i.e., h_L = 26 W m^{-2} K^{-1}, was adopted from previous studies involving external heating.[24] To determine the heat transfer coefficient between the sorbents and the wall, denoted as h_W, the regenerated contactors underwent heating to 100−105 °C with a N_2 purge to emulate regeneration conditions. The temperature profiles within the column during the experiment are illustrated in Figure S2 of the Supporting Information A sensitivity analysis conducted on h_W using the presented model resulted in h_W values of 10 W m^{-2} K^{-1} for the packed bed and 7 W m^{-2} K^{-1} for the monolith. The quality of these choices is illustrated in the red dashed curves in Figure S2, which depict the predicted column temperatures based on these coefficients.

2.5. Identifying the Limiting Mechanisms. While detailed adsorption modeling coupled with parameter estimation, as presented in Section 2.4, allows for the quantification of mass transfer and of axial dispersion effects, in this section, we introduce a simple methodology for qualitatively assessing these mechanisms solely from experimental results, without the need for a model.

The methodology centers around the analysis of the time interval from breakthrough to saturation of a compound being adsorbed, called Δt, after which the column reaches its equilibrium capacity. Such quantity, which can be viewed as the width of the breakthrough profile, is utilized as a measurable indicator of dispersion mechanisms, including mass transfer resistances and axial dispersion. Mass transfer effects are typically characterized by the Stanton number (St), while axial dispersion effects are characterized by the Peclet number (Pe), defined as $St = kL/u$ and $Pe = uL/D_L$, respectively. In equilibrium-controlled separations, mass transfer resistances and axial dispersion effects are negligible, resulting in infinitely large values of St and Pe and very sharp breakthrough profiles. In this scenario, Δt is infinitesimally small, and the breakthrough and saturation times coincide at the compound's mean residence time (t_{50}). In rate-controlled separations, finite values of St and Pe yield greater resistance, thus broadening the mass transfer zone and increasing the value of Δt. In such cases, column saturation is achieved at $t_{50} + \Delta t/2$. Consequently, saturating the bed comes at the expense of an extended adsorption time, and ceasing adsorption early results in under-utilization of the bed capacity. Both options lead to a decreased adsorption productivity, which is defined by the specific amount adsorbed

https://doi.org/10.1021/acs.iecr.4c01392
Ind. Eng. Chem. Res. 2024, 63, 11637−11653

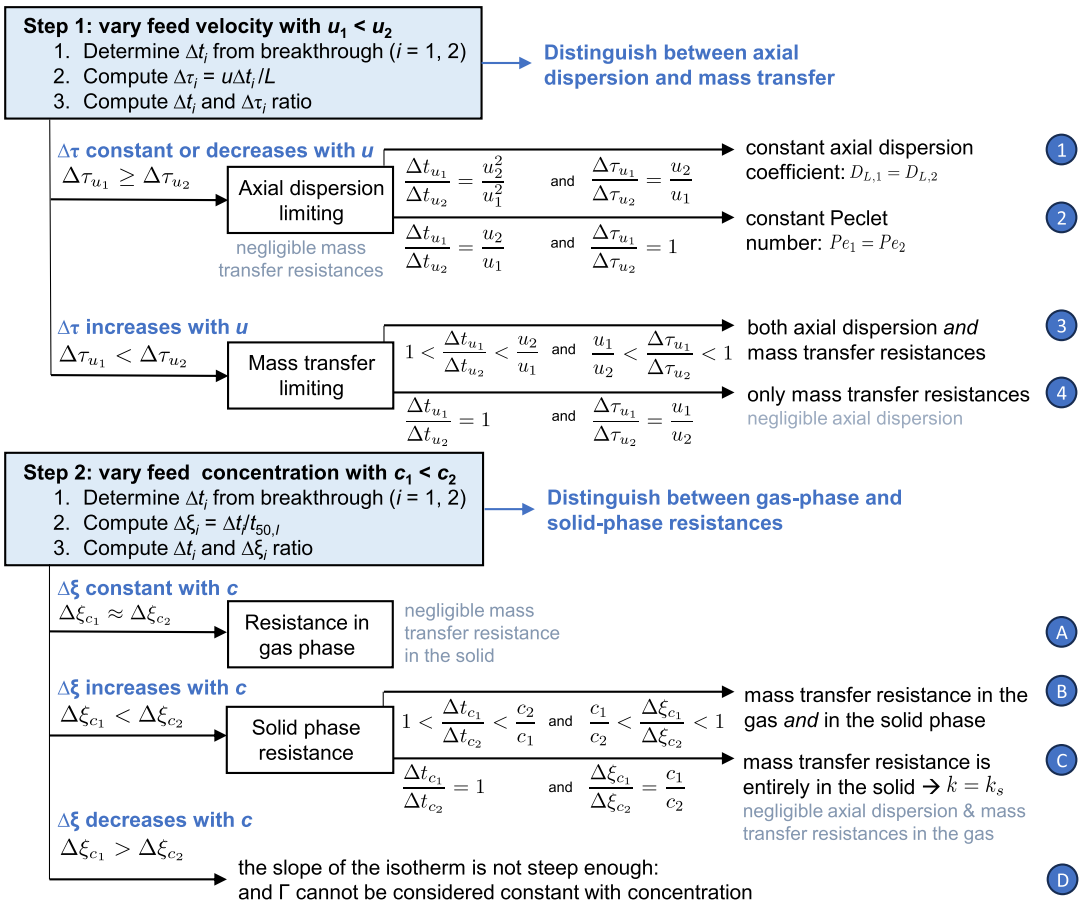

Figure 3. Schematic summary of a method, derived from a constant pattern analysis and described in Section S1, to determine the contribution of axial dispersion and the individual mass transfer resistances on the shape of a breakthrough profile through the variation of the feed velocity and of the feed concentration for sorbent with steep isotherms.

during adsorption. Because Δt serves as a tangible measure of kinetics and slower adsorption kinetics lead to decreased productivity, identifying the mechanisms contributing mostly to Δt is needed for enhancing productivity.

Illustrated in Figure 3, the methodology involves analyzing the breakthrough experiments conducted at various gas velocities and feed concentrations. The methodology stems from an analysis involving an analytical constant pattern solution, which is derived in detail in the Supporting Information and is applicable to sorbents with steep favorable isotherms. In the first step, the relevance of axial dispersion effects and mass transfer resistances is assessed by varying feed velocity and examining their effects on Δt and normalized time $\Delta\tau = u\Delta t/L$, as defined in Figure 3. In a second step, mass transfer resistances in the gas phase (associated with mass transport in the film and in the sorbent pores) and those in the solid phase are distinguished by varying the feed concentration and evaluating their influence on Δt and mass transfer zone $\Delta\xi = \Delta t/t_{50}$. This analytical method provides insights into the interplay of mass transfer and axial dispersion, shedding light on their relative contributions to the overall adsorption process.

2.6. Key Performance Indicators. The key performance indicators are measured in terms of specific energy consumption of the blower (W_{fan}, [MJ mol^{-1}]) and specific productivity (P, [mol kg^{-1} s^{-1}]) of the adsorption step, as defined below

$$W_{fan} = \frac{1}{q_{ads} m_s} \frac{1}{\eta_{fan}} \int_0^{t_{ads}} \dot{V}(p_{in} - p_{out})dt \quad (30)$$

$$P_{ads} = \frac{q_{ads}}{t_{ads}} \quad (31)$$

$$q_{ads} = \frac{\int_0^{t_{ads}} (\dot{n}_{in} - \dot{n}_{out})dt - n_{col}}{m_s} \quad (32)$$

$$n_{col} = \frac{y_{in} p_{col} \varepsilon^* V_{col}}{R T_{col}} \quad (33)$$

$$r = \frac{q_{ads} m_s}{\int_0^{t_{ads}} \dot{n}_{in} dt} \quad (34)$$

where m_s is the total sorbent mass, considering the total weight of the pellets or the weight of the entire monolith, $\eta_{fan} = 0.5$ is the efficiency of the blower, $\dot{V}$ is the volume flow rate of gas fed to the column, and $\dot{n}$ and p are the CO_2 molar flow rate and pressure, measured at the inlet and the outlet of the column. Here, q_{ads} ([mmol g$^{-1}_{sorbent}$]) represents the adsorbed phase concentration at time t_{ads}, which is the adsorption time to be considered in the calculation of the productivity and blower energy consumption. For the experiments conducted at 5.6%, we consider the maximum breakthrough time that allows a minimum CO_2 recovery rate of r = 95%, i.e., a suitable value for CO_2 capture from point-source capture. Since recovery rates do not impose restrictions on the duration of adsorption times in DAC, there is flexibility in deciding when to stop adsorption, and

https://doi.org/10.1021/acs.iecr.4c01392
Ind. Eng. Chem. Res. 2024, 63, 11637−11653

this point can be selected based on performance. For the experiments conducted at 400 ppm in this work, we choose $t_{ads} = t_{\alpha}$, where α represents the point at which $y = \alpha y_{in}$, and evaluate the impact of the choice of t_{ads} on adsorption productivity and specific blower energy requirements.

3. EXPERIMENTAL CAMPAIGN ON PACKED BEDS AND MONOLITHS

We have performed breakthrough experiments at two feed concentrations and multiple velocities, as presented in Section 3.1 and summarized in Table 5. To ensure the complete development of the breakthrough profile under all tested experimental conditions, velocities were maintained below 0.15 m/s. These velocities are possibly low compared to industrial DAC applications but are comparable to those encountered in the literature reporting similar experimental studies.[34−37,54,55] The specific ramifications of operating at higher velocities are further elucidated in Section 3.5.

Table 5. Operating Conditions of the Experimental Runs: Contactor Type, CO_2 mol Fraction in the Feed (y_{in}), Total Gas Molar Flow Rate of the Feed (n), and Gas Interstitial Velocity (u)

exp	y_{in} [-]	n [mmol s^{-1}]	u [m s^{-1}]
packed bed			
	400 ppm	2	0.14
	5.6%	2	0.14
	5.6%	1	0.07
	5.6%	0.5	0.04
monolith			
	400 ppm	3	0.13
	400 ppm	2	0.09
	400 ppm	1	0.04
	400 ppm	0.18	0.008
	5.6%	0.18	0.008
	5.6%	0.06	0.003
	5.6%	0.02	0.0009

In Section 3.1, we analyze the shape of the breakthrough curves and employ the methodology introduced in Section 2.5 to qualitatively identify the limiting adsorption mechanisms. In Section 3.2, we report the fit of the 1D model on the breakthrough experiments in terms of mass transfer and axial dispersion coefficients and compare the results to literature correlations.

3.1. Physical Interpretation of the Breakthrough Experiments. The breakthrough profiles of all experiments conducted are presented in Figure 4, in terms of the molar fraction of CO_2 at the column exit, y, and column temperature, T_{col}. The pressure drop measured across the contactors during each experiment is reported in Figure S3 of the Supporting Information. Only one experiment at 400 ppm of CO_2 in N_2 was conducted on the packed bed due to the high gas volume requirement for the experiment. As shown in Figure 4a, this resulted in the gas bottle being emptied and the breakthrough reaching only 90% of the feed concentration. Four velocities were tested at 400 ppm on the monolith, as shown in Figure 4c. Breakthrough experiments at 5.6% were conducted at three velocities on both the packed bed and the monolith, as illustrated in Figure 4b,d, respectively. Long, rather evident tails were observed in the breakthrough profiles of the monolith, while these were almost absent in the experiments at 5.6% feed concentration in the packed bed. The quantification and explanation of such a phenomenon are further discussed in Section 3.2.3. Good reproducibility of the experiments was verified by repeating three breakthrough experiments at 1 mmol s^{-1} on the packed bed at 5.6% and on the monolith at 400 ppm; the corresponding results are reported in Figure S4 of the Supporting Information.

3.1.1. Effect of Feed Velocity. Decreasing the velocity increased the spreading of the breakthrough curves and thus increased the Δt on both contactors. In Figure 5, we present the breakthrough data obtained at different velocities as a function of time, t, and normalized time, i.e., $\tau = tu/L$, with the time axis shifted so that the origin of the horizontal axis is at t_{50} or at τ_{50}. For the experiments conducted on the monolith at 5.6%, normalizing the data into τ resulted in a complete overlap of the breakthrough profiles and a constant $\Delta\tau$ at all velocities (Figure 5e). This correlates with case 2 of Figure 3, suggesting full control of the axial dispersion with a constant Peclet number. A constant $\Delta\tau$ was also observed at the two lower velocities of the experiments performed on the packed bed at 5.6%, after which $\Delta\tau$ increased (Figure 5d). This behavior indicated that these experiments operated at the limit of axial dispersion control, with both mass transfer resistances and axial dispersion becoming significant at higher velocities, as shown in case 3 of Figure 3. In the case of the 400 ppm monolith experiments, we observed an increase in $\Delta\tau$ with increasing velocity and $u_1/u_x < \Delta\tau_{u_1}/\Delta\tau_{u_x} < 1$, suggesting that both mechanisms contributed to Δt for all velocities (Figure 5f).

3.1.2. Effect of Feed Concentration. To assess the impact of feed concentration, we compared two experiments conducted at 2 mmol s^{-1} on the packed bed and two at 0.18 mmol s^{-1} on the monolith. Experiments at equal velocity were compared to ensure that any effects of axial dispersion and film resistance, if any, would equally influence both sets of experiments. Table 6 presents the CO_2 capacity at 90% breakthrough (q_{90}), the time to reach 90% breakthrough (t_{90}), and the mean residence time (t_{50}). Notably, the experiment at 400 ppm necessitated a mean residence time of 31 h, while nearly complete saturation took 45 h. Indeed, Δt was so large that it made up the entire breakthrough profile of Figure 4a, indicating exceptionally slow adsorption kinetics. Despite high heats of adsorption, the adsorption rate in this experiment was insufficient to generate a noticeable temperature peak, as was evident from the temperature profile. In contrast, at 5.6%, the breakthrough curve exhibited a considerably steeper slope, indicating significantly faster adsorption kinetics. This observation suggests a dependency of adsorption kinetics on the feed concentration. Indeed, although the total CO_2 equilibrium capacity was similar (0.44 and 0.71 mmol g^{-1} at 400 ppm and 5.6%, respectively), experiments at 5.6% resulted in temperature peaks exceeding 15 °C due to rapid adsorption rates. The comparison between 400 ppm and 5.6% feeds in the monolith contactor yielded analogous results regarding differences in Δt. Here, adsorption did not generate a significant temperature peak, due to the heat dissipation within the inert mass of the mullite support, representing 93.1 wt.% of the monolith, and to the active cooling provided by the monolith jacket.

Since both axial dispersion and mass transfer resistances were observed in the experiments at 5.6% on the packed bed and at 400 ppm in the monolith, we use the methodology presented in Figure 3 to distinguish between mass transfer resistances in the gas phase (associated with film and pore resistances) and in the

https://doi.org/10.1021/acs.iecr.4c01392
Ind. Eng. Chem. Res. 2024, 63, 11637−11653

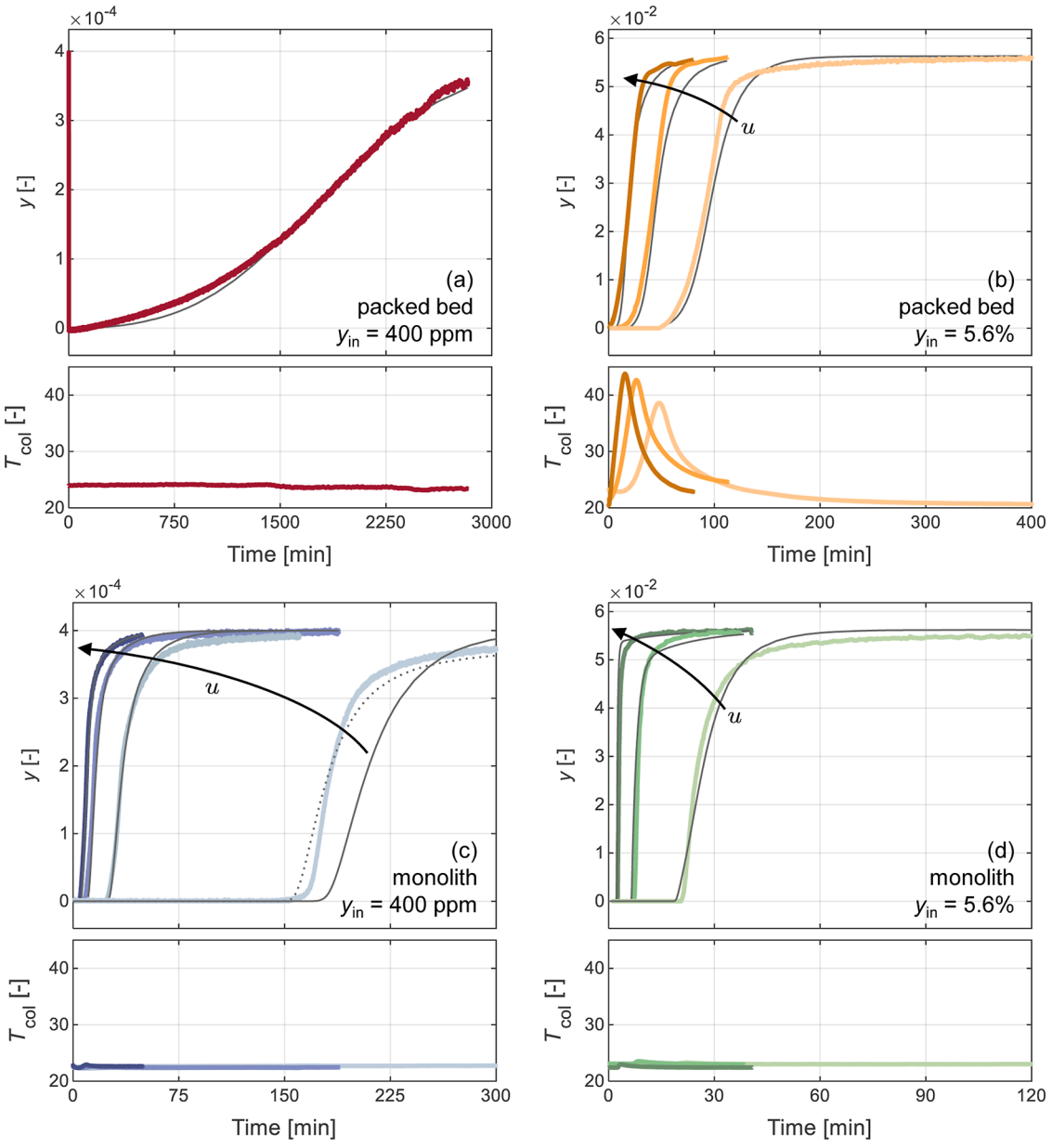

Figure 4. CO_2 breakthrough experiments (above) and the corresponding column temperature profiles (below) for experiments at: (a) y_{in} = 400 ppm on the packed bed at 2 mmol s^{-1}; (b) y_{in} = 5.6% on the packed bed at 2, 1 and 0.5 mmol s^{-1} (left to right); (c) y_{in} = 400 ppm on the monolith at 3, 2, 1 and 0.18 mmol s^{-1} (left to right); (d) y_{in} = 5.6% on the monolith at 0.18, 0.06 and 0.02 mmol s^{-1} (left to right). The thick lines in color are the experimental measurements, while the thin black lines are the simulation results with the DK model upon fitting, using estimated parameters as reported in Table 7. The dotted line in subfigure (c) for the rightmost experiment at 0.18 mmol s^{-1} corresponds to the DK model solution with $k_{s,amine}$ = 0.0001 s^{-1} instead of 0.0011 s^{-1} as in the simulations plotted as solid lines.

solid phase. The breakthrough curves obtained for the two feed concentrations on the packed bed and on the monolith at the same velocity are presented in Figure 6a,b, shifted with respect to t_{50}. The normalized breakthrough curves are shown underneath in Figure 6c,d, where the dimensionless time $(t - t_{50})/t_{50}$ is used as the axis such that the mass transfer zone thickness is equal to $\Delta\xi$. While the difference in steepness of the breakthrough profiles when plotted against t was obvious, when the curves at different concentrations were plotted against $(t - t_{50})/t_{50}$, they exhibited remarkable overlap, suggesting that $\Delta\xi_{400}/\Delta\xi_{5.6\%} \approx 1$. As shown in case A of Figure 3, this finding unequivocally eliminates the possibility of solid mass transfer resistances controlling adsorption and defining the breakthrough curve's shape.

In summary, the qualitative results of the mass transfer zone analysis revealed that, within the range of experimental conditions of this study: (i) axial dispersion played an important role in both the packed bed and the monolith experiments and (ii) any discernible mass transfer resistance predominantly occurred in the gas phase, with the solid resistance being negligible. Specifically, in all packed bed experiments and the experiment conducted at 400 ppm on the monolith, the shape of the breakthrough curve was influenced by the *combined* effects of mass transfer and axial dispersion (case 3A of Figure 3). However, at 5.6% on the monolith, only the effect of axial dispersion was observed (case 2A of Figure 3).

3.2. Modeling and Parameter Estimation. *3.2.1. PFO Model.* The estimated values of constant parameters k_g, k_s, p_1,

https://doi.org/10.1021/acs.iecr.4c01392
Ind. Eng. Chem. Res. 2024, 63, 11637−11653

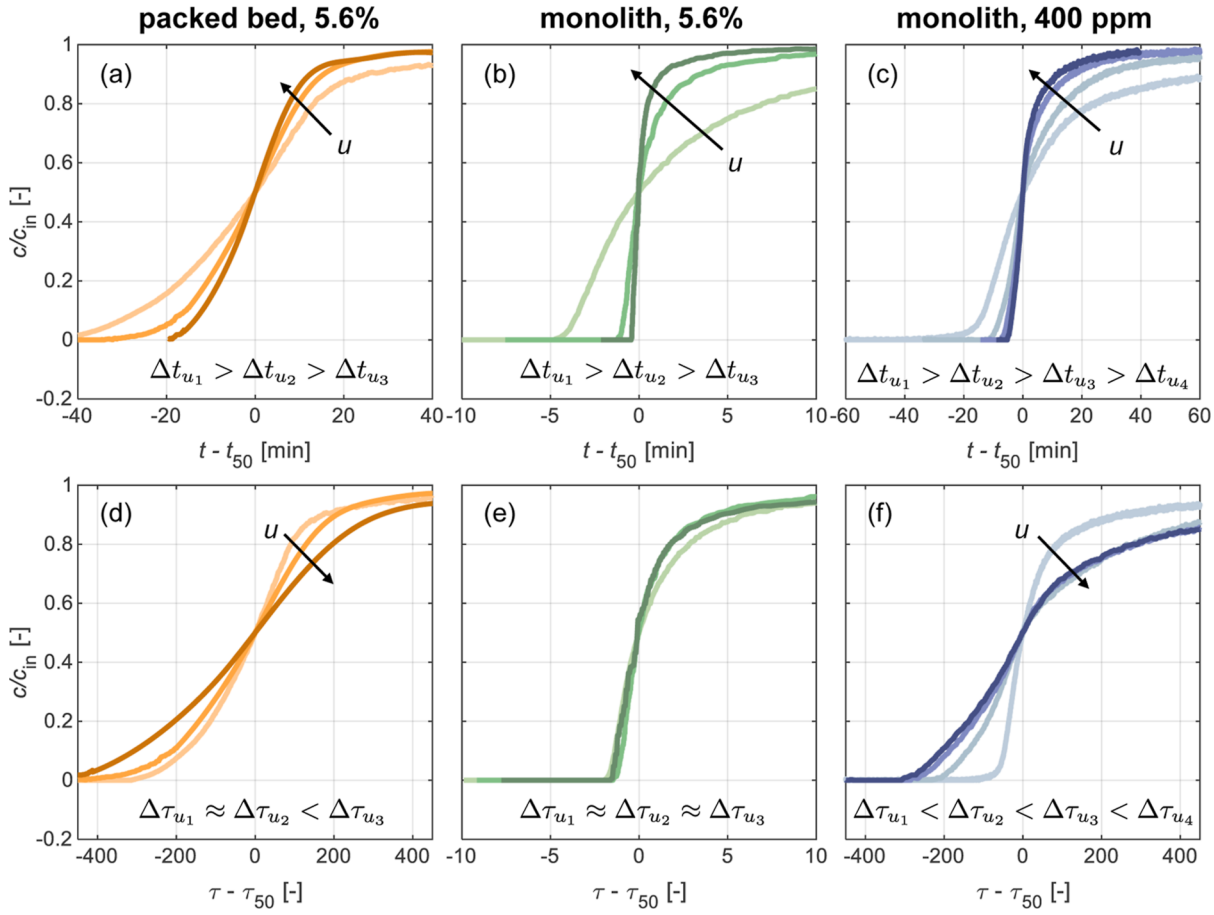

Figure 5. Effect of changing the feed velocity on the steepness of the breakthrough profiles, determined around t_{50} for (a–c) and around τ_{50} in the dimensionless time scale for (d–f).

Table 6. Values of q_{90}, t_{90}, and t_{50} for the Experiments Conducted at 2 mmol s^{-1} on the Packed Bed and 0.18 mmol s^{-1} on the Monolith

		packed bed		monolith	
		2 mmol s^{-1}		0.18 mmol s^{-1}	
	units	400 ppm	5.6%	400 ppm	5.6%
q_{90}	[mmol g^{-1}]	0.44	0.71	0.016	0.035
t_{90}	[s]	164,255	1960	14,964	258
t_{50}	[s]	110,389	1214	11,018	179

and p_2 on the packed bed, estimated using the procedure outlined in Section 2.4.5, are reported in Table 7. The estimated value of the axial dispersion coefficient is higher than those obtained from literature correlations. Although prior literature has shown that such correlations can often underestimate the axial dispersion coefficient,[56] such a major difference could stem from factors such as bypassing and channeling phenomena resulting from irregularities in the size and shape of the pellet rings (which might be too large for the column diameter). Despite the significant axial dispersion contribution, the optimizer effectively captured mass transfer resistances, and the minimization algorithm yielded values of k_g and k_s consistent with literature correlations. It was observed that variations in feed velocity had an insignificant effect on the film mass transfer coefficient, resulting in a constant k_g value for all experiments, which is also consistent with literature findings.[57] The major mass transfer resistance within k was found to be in the gas phase, consistent with the findings of constant pattern analysis.

Achieving a good fit using the PFO model for the monolith breakthrough curves proved to be impossible with any combination of k and D_L. To be more specific, the model was able to describe the initial part of the breakthrough profiles but unable to describe the long tails (see Figure 7). Therefore, resorting to the DK model was necessary to improve simulation accuracy.

3.2.2. Dual Kinetic Model. In the monolith experiments, fitting k_1 and D_L using the procedure presented in Section 2.4.5 resulted in multiple combinations, effectively describing the initial part of the breakthrough curve. Therefore, selecting appropriate k_1 and D_L involved utilizing literature correlations to compute k_1 and conducting a sensitivity analysis on D_L to estimate the values of p_1 and p_2, as reported in Table 7. Axial dispersion was again significantly higher than that from literature correlations. This indeed confirms the constant pattern findings and could be attributed to gas channeling around and through the textile felts, which keep the monolith in place.

Subsequently, k_2 and η were fitted to the entire breakthrough profile of the monolith experiments. The fraction of surface amine sites was found to be $\eta = 0.75$ and the amine layer rate constant was fitted to eq 13, yielding $k_{s,amine} = 0.0011\ s^{-1}$. The resulting k_1 and k_2 values are reported in Table 8, and the DK model simulations using the fitted parameters are plotted as gray curves in Figure 4. The DK model simulations with the fitted parameters effectively reproduced the monolith breakthrough

https://doi.org/10.1021/acs.iecr.4c01392
Ind. Eng. Chem. Res. 2024, 63, 11637−11653

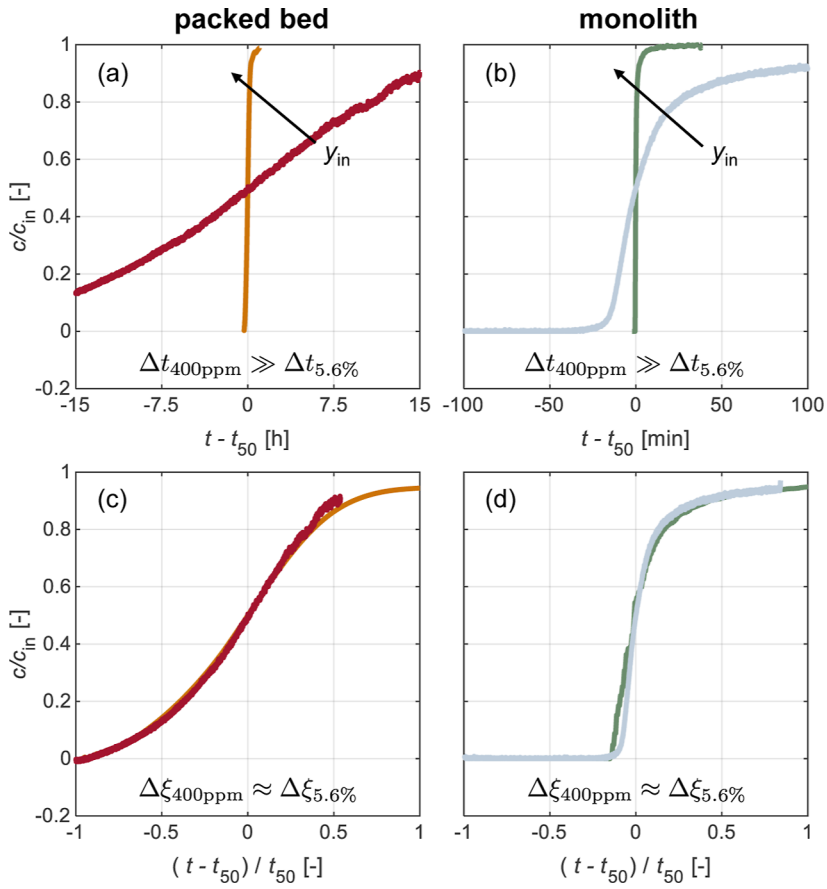

Figure 6. Comparison of breakthrough profiles at two different feed concentrations: orange and green curves at 5.6%, and red and blue curves at 400 ppm. The concentrations were evaluated under constant velocity conditions: 2 mmol s^{-1} on the packed bed and 0.18 mmol s^{-1} on the monolith. Subfigures (a,b) represent the time axis in minutes, while (c,d) show a normalized time axis.

Table 7. Transport Parameters Estimated on the Two Contactors and Comparison with Literature Correlations Reported in Table 4, with the Interstitial Velocity, u, Expressed in $[m\ s^{-1}]$

		packed bed		monolith	
	units	estimate	literature	estimate	literature
k_f	$[s^{-1}]$	—	43−70	—	93
k_p	$[s^{-1}]$	—	3.35	—	237
k_g	$[s^{-1}]$	2.79	3.19	—	67
k_s	$[s^{-1}]$	5.8×10^5	1.9×10^4	—	1.9×10^4
$k_{s,amine}$	$[s^{-1}]$	—	—	0.0011	—
η	[—]	—	—	0.75	—
D_L	$[m^2\ s^{-1}]$	$6.95u + 0.02$	$0.0015u + 0.00003$	$1.22\ u^2 + 0.0004$	$0.0013\ u^2 + 0.0000162$

curves and their tail behavior, with the exception of the 0.18 mmol s^{-1} experiment in Figure 4c. Adjusting $k_{s,amine}$ to 0.0001 s^{-1} improved the overall fit (shown by the dotted gray line). This observation does not resolve the issue that this specific experiment cannot be described with the same parameters as the others, but at least it proves that the DK model is in general capable of describing the type of asymmetric breakthrough profiles so clearly observed in the case of monoliths.

3.2.3. Comparing the PFO and DK Model Solutions. The successful application of the PFO model in modeling the packed bed experiments suggests that employing a DK model may not be necessary for this contactor. Indeed, attempts to use the DK model in fitting the packed bed breakthrough profiles resulted in: $k_2 = k_1$, for any value of η; or $\eta = 1$ for any value of k_2, leading to the same solution as the PFO model. Assuming that the physical characteristics of the amine layer in the γ-alumina phase of both contactors are the same, we applied the η and $k_{s,amine}$ values estimated on the monolith to test the DK model's performance in the packed bed simulations. The solutions obtained with PFO and DK models are similar, as shown in Figure 7a. Despite the likely existence of two types of amine sites in the pellets, the slow rate of mass transport to the surface amines (k_1) compared to that of mass transport in the aminopolymer layer ($k_{s,amine}$) renders the influence of $k_{s,amine}$ on k_2 minimal. This results in comparable magnitudes of k_1 and k_2, causing an insignificant change in mass transfer kinetics and explaining the absence of an evident tail in the simulations and in the experiments in packed beds.

In contrast to the packed bed experiments, the kinetics within the aminopolymer layer significantly affected k_2 in the

https://doi.org/10.1021/acs.iecr.4c01392
Ind. Eng. Chem. Res. 2024, 63, 11637−11653

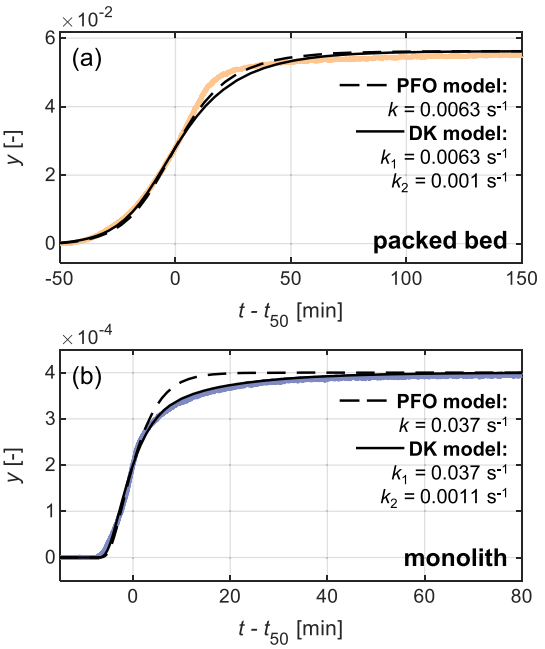

Figure 7. Comparison between the DK model (solid) and the PFO model (dashed) solutions with k_1 and k_2 as defined in Table 8 and $k = k_1$ on the (a) packed bed, at 5.6% and 0.5 mmol s^{-1}; (b) monolith, at 400 ppm and 2 mmol s^{-1}

Table 8. Values of c_{in}/q^*_{in} for the Four Experiment Types Spanning Across Two Contactors and Two Feed Concentrations and Resulting Values of k_1 and k_2 Computed from eqs 12 and 13 Using the Estimated Mass Transfer Coefficients Reported in Table 7

		packed bed		monolith	
	units	400 ppm	5.6%	400 ppm	5.6%
c_{in}/q^*_{in}	[-]	0.00003	0.002	0.0006	0.04
k_1	[s^{-1}]	0.000088	0.0063	0.037	2.7
k_2	[s^{-1}]	0.000082	0.001	0.0011	0.0011

monoliths, owing to the considerably larger value of k_1 compared to $k_{s,amine}$. This resulted in a substantial change in mass transfer kinetics during adsorption, which was particularly evident at higher concentrations, where the tail was more pronounced and the difference between k_1 and k_2 was even larger. This disparity explains why the tails were more pronounced on the monoliths than on the packed bed, highlighting the inadequacy of the PFO model in capturing this effect (Figure 7b). Nevertheless, for cases in which reaching full saturation is not favorable, detailed modeling of breakthroughs beyond the start of elongated tails may not be essential, especially for cyclic modeling. To this end, using a PFO model to capture the curve's initial slope until the desired saturation point may suffice.

3.3. Contactor Comparison. *3.3.1. Assessment of the Resulting Mass Transfer Kinetics.* Several observations can be made based on the estimated mass transfer coefficients and their comparison with literature correlations. First, k_s is much larger than k_g, thus k_1 is controlled by the resistance in the gas phase (film and sorbent pores). This is consistent with the findings of the constant pattern analysis. As a result, mass transfer kinetics are concentration-dependent, with k_1 proportional to $c_{in}/q^*_{p,in}$ (Table 8). Moreover, in the packed bed k_g is determined by k_p whereby k_f plays a negligible role; in the monolith instead both k_p and k_f influence k_g within the specified range of velocities. Operating at higher feed velocities on the monolith would decrease the impact of k_f, resulting in k_1 being only governed by k_p. Comparing the two contactors, k_1 was approximately 400 times higher on the monolith than on the packed bed. This is due to a higher value of $c_{in}/q^*_{p,in}$ in the monolith and to several geometric differences: the reduced wall thickness of the monolith compared to the diameter of the pellet (shorter diffusion path in k_p); and the monolith's macroporous structure (faster diffusivity in k_p).

3.3.2. Adsorption KPIs. Despite the monolith's significantly lower CO_2 capacity, i.e., 0.016 mmol g^{-1} compared to 0.44 mmol g^{-1} in the packed bed, the reduction in diffusion path offered by the monolith presents a promising strategy to mitigate mass transfer limitations. To assess the tradeoff between mass transfer kinetics and CO_2 capacity, the adsorption productivity and the specific blower energy consumption were computed, thus obtaining the values plotted in Figure 8a for all experiments performed at 400 ppm. The KPIs were calculated at various

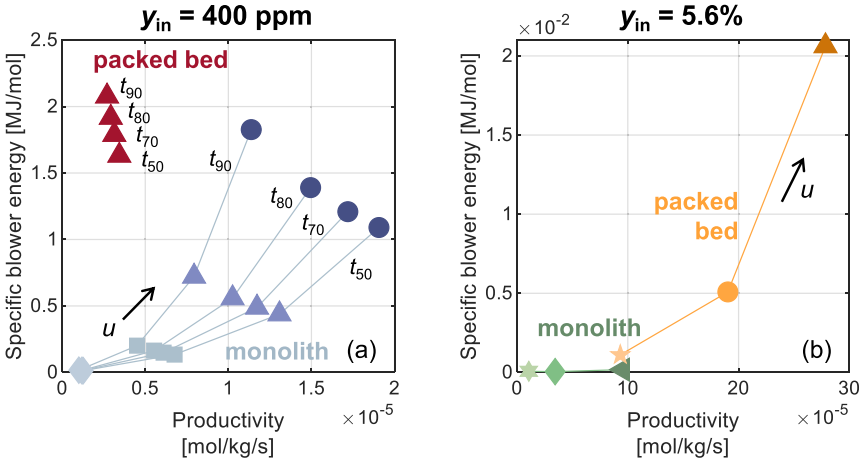

Figure 8. Specific energy demand plotted against the productivity of the adsorption step and comparison between the packed bed and monolith for all of the experiments performed in this study using a CO_2 inlet molar fraction of (a) y_{in} = 400 ppm; (b) y_{in} = 5.6%. The curves in subfigure (a) show the evolution of the blower energy consumption vs productivity when defining the total adsorption time at 90, 80, 70, and 50% of the breakthrough, defined as t_{90}, t_{80}, t_{70}, and t_{50}, respectively; the curves in subfigure (b) respect a recovery rate constraint of 95%.

https://doi.org/10.1021/acs.iecr.4c01392
Ind. Eng. Chem. Res. 2024, 63, 11637−11653

points along the breakthrough curve to assess the effect of saturation on performance, as achieving full saturation of the column may not optimize the performance. The productivity-energy values obtained by varying velocities on the monolith indicate that there is a tradeoff between productivity and energy penalty (associated with the operation of the blower), which both increase with increasing gas velocities. Notably, the results illustrated in Figure 8 indicate that at t_{90}, at the same flow rate of 2 mmol s^{-1}, the use of a monolith resulted in a 50% reduction in specific blower energy consumption and a 66% increase in productivity compared to a packed bed. This observation implied that increased mass transfer rates on the monolith more than compensated for its reduction in the CO_2 capacity. Stopping adsorption early improved our KPIs, as adsorption productivity drops as soon as breakthrough is reached. While full column saturation seems unfavorable, definitive conclusions on adsorption times require consideration of the whole DAC cycle. Importantly, the qualitative comparison between contactors remains consistent at different points of saturation. It is worth noting that, using productivity per unit volume occupied by each contactor, our findings exhibited the same trends, as shown in Figure S5.

Figure 8b shows the curves for the experiments performed at 5.6%, at three velocities both on the packed bed and on the monolith. The only difference from the experiments at 400 ppm consisted of the requirement that a minimum CO_2 recovery rate of 95% was fulfilled, as highlighted in Section 2.6. Interestingly, the conclusions drawn for the DAC-relevant conditions were less evident at the higher feed concentration: transitioning from the packed bed to the monolith did not result in an unequivocally better performance during adsorption. These observations suggest that, although the mass transfer coefficient on the monolith was indeed larger than that on the packed bed, the decrease in the CO_2 capacity in the monolith could not be offset by the faster kinetics as in the case of the 400 ppm experiments. Although these results are specific to the experiments conducted in this work, they highlight the importance of selecting the appropriate material and contactor for each given separation process.

3.4. Regeneration Experiments. Though the focus of this study is on the adsorption step, during sorbent regeneration, i.e., a routine operation after saturating the contactor at the selected feed concentration), we recorded elution profiles and outlet temperature. Representative regeneration profiles after adsorption at 400 ppm and 5.6% performed on the packed bed column and on the monolith are presented in Figure 9a,b, respectively, where the rate of outflowing CO_2 and the temperature are plotted. As described in the methodology section (Section 2), CO_2 desorption and column regeneration require both purge with N_2 (or evacuation) and heating, as also reported earlier.[58]

Without carrying out an in-depth discussion of the regeneration step in the context of the entire DAC cycle, which is beyond the scope of this work, it is worth observing in the figures that regeneration times are similar in the same contactor for the two quite different concentration levels, namely, about 2 h for fixed beds and less than 1 h for monoliths. This is in obvious contrast to adsorption times, which are very different for the two concentration levels; as reported in Table 6, t_{90} for adsorption is about 80 and 60 times larger at 440 ppm than at 5.6% in packed beds and in monoliths, respectively. This difference between adsorption and regeneration stems from the fact that the equilibrium adsorbed amount at the two very different feed concentrations in the gas (5.6% is about 150 times

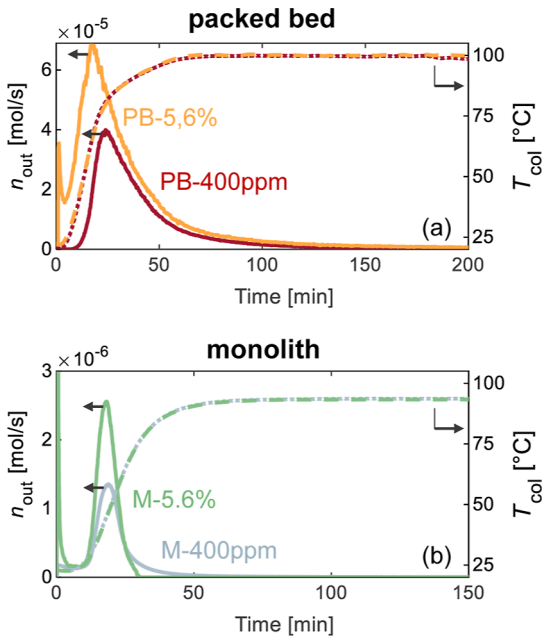

Figure 9. Experimental regeneration profiles on the packed bed (PB) and on the monolith (M) after experiments performed with a feed of y = 400 ppm and y = 5.6%, showing the molar outflow of CO_2 (solid line) and the column temperature (dotted or dashed line).

larger than 400 ppm) differs by only about 50% (from 0.44 mmol g^{-1} at 400 ppm to 0.71 mmol g^{-1} at 5.6%).

On the one hand, when one looks at regeneration as a thermal swing step, the heat requirement is due to the need of heating adsorbent and contactor, which is the same whatever the initial concentration, and to the need to desorb the saturation amount of CO_2, whose contribution is small and differs only slightly for the two concentration levels. On the other hand, the amount of CO_2 to be adsorbed, which is of the same order of magnitude at 400 ppm and at 5.6%, is conveyed into the contactor at widely different rates indeed because of the widely different concentrations, even when the gas velocity is the same in the two cases. Such material balance effect is combined with the role played by the adsorption isotherm at the initial and final temperature of the swing step, thus yielding almost 2 orders of magnitude of difference in the adsorption times between low and high CO_2 concentration in the feed.

The following figures quantify this effect: at 5.6%, the adsorption step accounts for about 15% of the total adsorption and regeneration cycle time, while at 400 ppm, it accounts for about 90% of the overall time. Interestingly, we observe that the ratio is similar in Climeworks' ORCA plant, where the adsorption step occupies 83% of the total cycle time.[59]

3.5. Contextualizing This Work in DAC-Relevant Conditions. To contextualize our findings for DAC-relevant conditions, it is essential to also consider factors such as the influence of humidity in the feed and the impact of operating at higher velocities.

While air humidity was not explicitly addressed in this study, literature has documented an increase in CO_2 adsorption capacity by water coadsorption on amine-functionalized materials.[10,60] The quantitative impact of water coadsorption on the KPIs considered here remains uncertain, because it may impact both CO_2 capacity (by improving it) and mass transfer kinetics (by slowing it down).[61] To effectively evaluate this, one must conduct equilibrium and kinetic measurements on CO_2−

https://doi.org/10.1021/acs.iecr.4c01392
Ind. Eng. Chem. Res. 2024, 63, 11637−11653

H_2O coadsorption, coupled with cyclic DAC studies. Nonetheless, we anticipate that the introduction of humidity in the feed would affect the two contactors similarly and would yield a qualitatively similar comparison to that illustrated in Figure 8.

Axial dispersion and mass transport in the gas film and sorbent pores control adsorption within our experimental framework. Operating at higher velocities mitigates limitations arising from axial dispersion and film resistance, leading to an improvement in the separation performance. However, this improvement is limited by mass transport in the sorbent pores, which is a sorbent property independent of the velocity. Thus, regardless of the feed velocity, the thin monolith walls offer a diffusion length that enhances mass transport compared to pellets of a relevant size. This provides a practical solution to enhance the DAC kinetics.

4. CONCLUSIONS

In this work, we considered two amine-functionalized γ-alumina sorbents in the shape of pellets and a γ-alumina wash-coated monolith. We performed multiple breakthrough experiments on a cylindrical packed bed containing the pellets and on the monolith, with the goal of: (i) gaining insight on the mechanisms limiting adsorption kinetics, (ii) quantifying the transport phenomena with detailed adsorption modeling, and (iii) comparing the adsorption performance of the two contactors within the range of experimental conditions studied. The work resulted in the following key insights.

- The mass transfer zone analysis using the constant pattern revealed, without the need for a physical model, that the dominant mass transfer resistances are in the gas film and in the pores. Moreover, significant axial dispersion was observed, particularly at higher concentrations, thus highlighting its impact on system performance where mass transfer resistances were smaller. While the broadness of the mass transfer front is not a concern for CO_2 recovery in DAC applications, proper column design to avoid such phenomena is necessary to ensure optimal utilization of the contactor;
- Subsequently, the 1D model was employed to estimate transport parameters during adsorption. Here, the qualitative findings of the constant pattern analysis were confirmed and mass transfer correlations were validated. However, a notable discrepancy in the estimated and literature axial dispersion coefficients indicated the possible occurrence of gas bypassing within the contactors;
- Two mass transfer models were evaluated: a conventional pseudo-first-order model and a dual kinetic model, which incorporates two types of amine sites with distinct saturation capacities and rates of mass transfer. Implementation of the DK model revealed that the kinetics in the aminopolymer layer are considerably slower than mass transport in the gas film and in the pores of the monolith. This explained the elongated breakthrough tails and confirmed the need to use such a model to adequately describe this behavior. In contrast, slow mass transport in film and sorbent pores in packed bed experiments governed adsorption, resulting in negligible influence of mass transfer resistances in the aminopolymer. This explained the lack of evident tails in the packed bed experiments and validated the use of a PFO model for their description;
- The obtained results demonstrated that the monolith contactor exhibited significantly higher mass transfer coefficients compared to packed beds, which can be attributed to the combined effects of shorter diffusion lengths (0.4 mm walls vs 3 mm pellets) and lower equilibrium capacity, resulting in higher values of the factor $c_{in}/q^*_{p,in}$;
- As a result, experiments at 400 ppm performed on the monolith exhibited reduced specific energy consumption and an increase in adsorption productivity with respect to the packed bed, thus making the monolith the preferred contactor for such a separation within the range of experimental conditions studied. The increased mass transfer coefficient on the monolith was not sufficient to simultaneously increase productivity and specific energy consumption of the blower at 5.6% with respect to the packed bed, thus not allowing for a clear choice regarding the preferred contactor for such conditions.

In the past, research on monoliths as promising contactors for DAC were motivated by the possibility to reduce the significant electrical energy consumption associated with high pressure drops, typical of packed beds. However, recent studies have indicated that monoliths possess additional advantageous geometric properties that can lead to improved mass transfer rates. By investigating and elucidating these phenomena, this research contributes to a comprehensive understanding of the enhanced mass transfer in monolith contactors, highlighting their crucial role in DAC systems.

■ ASSOCIATED CONTENT

Supporting Information

The Supporting Information is available free of charge at https://pubs.acs.org/doi/10.1021/acs.iecr.4c01392.

Additional information on the measured equilibrium data, heat transfer coefficients, measured pressure drop, experiment reproducibility, and key performance indicators and derivation of Figure 3 (PDF)

■ AUTHOR INFORMATION

Corresponding Author

Marco Mazzotti − *Institute of Energy and Process Engineering, ETH Zurich, Zurich 8092, Switzerland;* orcid.org/0000-0002-4948-6705; Phone: +41 44 632 24 56; Email: marco.mazzotti@ipe.mavt.ethz.ch; Fax: +41 44 632 11 41

Authors

Valentina Stampi-Bombelli − *Institute of Energy and Process Engineering, ETH Zurich, Zurich 8092, Switzerland*

Alba Storione − *Department of Civil, Chemical, Environmental and Materials Engineering (DICAM), Alma Mater Studiorum-University of Bologna, Bologna 40131, Italy*

Quirin Grossmann − *Institute of Energy and Process Engineering, ETH Zurich, Zurich 8092, Switzerland;* orcid.org/0000-0003-0999-0891

Complete contact information is available at: https://pubs.acs.org/10.1021/acs.iecr.4c01392

Notes

The authors declare no competing financial interest.

https://doi.org/10.1021/acs.iecr.4c01392
Ind. Eng. Chem. Res. 2024, 63, 11637−11653

■ ACKNOWLEDGMENTS

We would like to thank HUG Engineering, and Michael Pabel and his co-workers at Saint Gobain for providing the samples used in this work. This work was supported by the Swiss National Science Foundation grant number 197221.

■ NOTATION

Roman symbols

A	column cross section [m^2]
c	gas phase concentration [mol m^{-3}]
d_p	pellet diameter [m]
d_{pore}	diameter of the γ-alumina pore [m]
D	column diameter [m]
D_{al}	effective diffusivity in the γ-alumina pockets [m^2 s^{-1}]
D_p	effective diffusivity in the pellet pore [m^2 s^{-1}]
D_m	molecular diffusion v[m^2 s^{-1}]
$D_{mullite}$	effective diffusivity in the mullite pores [m^2 s^{-1}]
D_s	crystalline diffusivity [m^2 s^{-1}]
D_L	axial dispersion coefficient [m^2 s^{-1}]
k	LDF overall mass transfer coefficient [s^{-1}]
K	Langmuir equilibrium constant [m^3 mol^{-1}]
k_f	film mass transfer coefficient [s^{-1}]
k_f'	film mass transfer coefficient [m s^{-1}]
k_p	pore mass transfer coefficient [s^{-1}]
$k_{p,al}$	mass transfer coefficient in the γ-alumina pocket mesopores [s^{-1}]
$k_{p,mullite}$	mass transfer coefficient in the mullite macropores [s^{-1}]
k_s	solid mass transfer coefficient [s^{-1}]
L	column length [m]
M	molecular weight [g mol^{-1}]
m_s	sorbent mass [kg]
$\dot{n}$	molar flow rate [mol s^{-1}]
N	total number of cells in the monolith [-]
p	pressure [Pa]
Pe	Peclet number, [$=uL/D_L$] [-]
q	mass-based adsorbed-phase concentration [mol $kg^{-1}_{sorbent}$]
q_p	volume-based adsorbed-phase concentration, [$=q\rho_p$] [mol m^{-3}]
$\hat{q}$	volume-based adsorbed-phase concentration, [$=q\rho_s$] [mol m^{-3}]
q^*	solid loading at equilibrium with c [mol kg^{-1}]
r_1	internal hydraulic diameter of the square monolith channel,[50] [$=2w_1/\pi$] [m]
r_2	external hydraulic diameter of the square monolith channel,[50] [$= (4w_{wall}w_2/pi + r_1^2)^{0.5}$] [m]
r_{al}	radius of γ-alumina pockets [m]
r_c	crystalline radius [m]
r_p	pellet radius [m]
Re	Reynolds number, [$=\rho u_s d_p/\mu$] [-]
Sc	Schmidt number, [$=\mu/(\rho D_m)$] [-]
Sh	Sherwood number [-]
St	Stanton number, [$=kL/u$] [-]
t	time [s]
T	temperature [K]
u	interstitial velocity, [$=u_s/\varepsilon$] [m s^{-1}]
u_s	superficial velocity [m s^{-1}]
$\dot{V}$	volumetric flow rate of the gas feed [m^3 s^{-1}]
W	monolith width [m]
w_1	monolith void channel width [m]
w_2	monolith cell width, [$w_2 = w_1 + w_{wall}$] [m]
W_{fan}	specific blower energy consumption [MJ mol^{-1}]
w_{wall}	monolith wall thickness [m]
x	dimensionless axial coordinate, [$=z/L$] [-]
y	CO_2 molar fraction [-]
z	axial coordinate [m]

Greek Symbols

α	parameter of the shock layer [-]
β	percentage of the feed concentration in the shock layer analysis v[-]
Δp	pressure drop across the column [Pa]
ε	bed void fraction [-]
ε_{al}	void fraction of the γ-alumina pockets in the monolith [-]
ε_p	pellet/wall void fraction [-]
ε^*	total void fraction, [$=\varepsilon + \varepsilon_p(1-\varepsilon)$] [-]
Γ	parameter of the shock layer [-]
λ	dimensionless shock velocity [-]
μ	dynamic viscosity [Pa s]
ν	capacity ratio, [$=(1-\varepsilon)/\varepsilon$] [-]
ν^*	capacity ratio, [$=(1-\varepsilon^*)/\varepsilon^*$] [-]
ξ	moving coordinate, [$= z - \lambda\tau$] [-]
ψ	porosity ratio, [$=\varepsilon^*/\varepsilon$] [-]
ρ_b	bed density [kg m^{-3}_{COLUMN}]
ρ_p	pellet density [kg m^{-3}_{PELLET}]
ρ_s	solid density [kg m^{-3}_{SOLID}]
τ	dimensionless time, [$=tu/L$] [-]
τ_{al}	γ-alumina tortuosity [-]
$\tau_{mullite}$	mullite tortuosity [-]
ϑ	parameter of the shock layer [-]

Subscripts and Superscripts

in feed conditions

Acronyms

CPSI	cells per square inch
DAC	direct air capture
KPI	key performance indicator
LDF	linear driving force
MFC	mass flow controller
MTZ	mass transfer zone
NET	negative emission technologies

■ REFERENCES

(1) United Nations Environment Programme, Paris Agreement. 2015. https://wedocs.unep.org/20.500.11822/20830 (accessed: Jan 10, 2023).

(2) EASAC. *Negative Emission Technologies: What Role in meeting Paris Agreement Targets?*; EASAC, 2018; p 37.

(3) Sodiq, A.; Abdullatif, Y.; Aissa, B.; Ostovar, A.; Nassar, N.; El-Naas, M.; Amhamed, A. A review on progress made in direct air capture of CO_2. *Environ. Technol. Innov.* **2023**, *29*, 102991.

(4) Sabatino, F.; Grimm, A.; Gallucci, F.; van Sint Annaland, M.; Kramer, G. J.; Gazzani, M. A comparative energy and costs assessment and optimization for direct air capture technologies. *Joule* **2021**, *5*, 2047−2076.

(5) Sanz-Pérez, E. S.; Murdock, C. R.; Didas, S. A.; Jones, C. W. Direct Capture of CO_2 from Ambient Air. *Chem. Rev.* **2016**, *116*, 11840−11876.

(6) Barkakaty, B.; Sumpter, B. G.; Ivanov, I. N.; Potter, M. E.; Jones, C. W.; Lokitz, B. S. Emerging materials for lowering atmospheric carbon. *Environ. Technol. Innov.* **2017**, *7*, 30−43.

(7) Belmabkhout, Y.; Serna-Guerrero, R.; Sayari, A. Adsorption of CO_2-Containing Gas Mixtures over Amine-Bearing Pore-Expanded MCM-41 Silica: Application for Gas Purification. *Ind. Eng. Chem. Res.* **2010**, *49*, 359−365.

https://doi.org/10.1021/acs.iecr.4c01392
Ind. Eng. Chem. Res. 2024, 63, 11637−11653

(8) Choi, S.; Gray, M. L.; Jones, C. W. Amine-tethered solid adsorbents coupling high adsorption capacity and regenerability for CO2 capture from ambient air. *ChemSusChem* **2011**, *4*, 628−635.
(9) Kwon, H. T.; Sakwa-Novak, M. A.; Pang, S. H.; Sujan, A. R.; Ping, E. W.; Jones, C. W. Aminopolymer-Impregnated Hierarchical Silica Structures: Unexpected Equivalent CO_2 Uptake under Simulated Air Capture and Flue Gas Capture Conditions. *Chem. Mater.* **2019**, *31*, 5229−5237.
(10) Gebald, C.; Wurzbacher, J. A.; Tingaut, P.; Zimmermann, T.; Steinfeld, A. Amine-based nanofibrillated cellulose as adsorbent for CO_2 capture from air. *Environ. Sci. Technol.* **2011**, *45*, 9101−9108.
(11) Lee, J. J.; Yoo, C. J.; Chen, C. H.; Hayes, S. E.; Sievers, C.; Jones, C. W. Silica-Supported Sterically Hindered Amines for CO_2 Capture. *Langmuir* **2018**, *34*, 12279−12292.
(12) Gebald, C.; Wurzbacher, J. A.; Borgschulte, A.; Zimmermann, T.; Steinfeld, A. Single-Component and Binary CO_2 and H2O Adsorption of Amine-Functionalized Cellulose. *Environ. Sci. Technol.* **2014**, *48*, 2497−2504.
(13) Darunte, L. A.; Oetomo, A. D.; Walton, K. S.; Sholl, D. S.; Jones, C. W. Direct Air Capture of CO_2 Using Amine Functionalized MIL-101(Cr). *ACS Sustainable Chem. Eng.* **2016**, *4*, 5761−5768.
(14) Darunte, L. A.; Terada, Y.; Murdock, C. R.; Walton, K. S.; Sholl, D. S.; Jones, C. W. Monolith-Supported Amine-Functionalized Mg2(dobpdc) Adsorbents for CO_2 Capture. *ACS Appl. Mater. Interfaces* **2017**, *9*, 17042−17050.
(15) Young, J., García-Díez, E., Garcia, S., Ireland, C., Smit, B., van der Spek, M. Investigating H_2O and CO_2 co-adsorption on amine-functionalised solid sorbents for direct air capture. In *SSRN Electronic Journal*, 2021; pp 1−7.
(16) Rezaei, F.; Webley, P. Optimum structured adsorbents for gas separation processes. *Chem. Eng. Sci.* **2009**, *64*, 5182−5191.
(17) Rezaei, F.; Webley, P. Structured Adsorbents in Gas Separation Processes. *Sep. Purif. Technol.* **2010**, *70*, 243−256.
(18) Mennitto, R.; Sharma, I.; Brandani, S. Extruded monoliths for gas separation processes: Height equivalent to a theoretical plate and pressure drop correlations. *AlChE J.* **2022**, *68*, No. e17650.
(19) Gebald, C.; Piatkowski, N.; Rüesch, T.; Wurzbacher, J. A. Low-Pressure Drop Structure of Particle Adsorbent Bed for Adsorption Gas Separation Process. WO 2014/170184 Al, 2014.
(20) Yu, Q.; Brilman, W. A Radial Flow Contactor for Ambient Air CO2 Capture. *Appl. Sci.* **2020**, *10*, 1080.
(21) Eisenberger, P.; Chichilnisky, G. Rotating Multi-Monolith Bed Movement System for Removing CO_2 from the Atmosphere. U.S. Patent: 10,512,880 B2, 2019.
(22) Eisenberger, P. Carbon Dioxide Capture/Regeneration Structures and Techniques. U.S. Patent: 8,163,066 B2, 2012.
(23) Kulkarni, A. R.; Sholl, D. S. Analysis of equilibrium-based TSA processes for direct capture of CO_2 from Air. *Ind. Eng. Chem. Res.* **2012**, *51*, 8631−8645.
(24) Stampi-Bombelli, V.; van der Spek, M.; Mazzotti, M. Analysis of direct capture of CO_2 from ambient air via steam-assisted temperature−vacuum swing adsorption. *Adsorption* **2020**, *26*, 1183−1197.
(25) Balasubramaniam, B. M.; Thierry, P.-T.; Lethier, S.; Pugnet, V.; Llewellyn, P.; Rajendran, A. Process-performance of solid sorbents for Direct Air Capture (DAC) of CO_2 in optimized temperature-vacuum swing adsorption (TVSA) cycles. *Chem. Eng. J.* **2024**, *485*, 149568.
(26) Sinha, A.; Darunte, L. A.; Jones, C. W.; Realff, M. J.; Kawajiri, Y. Systems Design and Economic Analysis of Direct Air Capture of CO_2 through Temperature Vacuum Swing Adsorption Using MIL-101(Cr)-PEI-800 and mmen-Mg2(dobpdc) MOF Adsorbents. *Ind. Eng. Chem. Res.* **2017**, *56*, 750−764.
(27) Sinha, A.; Realff, M. J. A parametric study of the techno-economics of direct CO_2 air capture systems using solid adsorbents. *AlChE J.* **2019**, *65*, 1−8.
(28) Fasihi, M.; Efimova, O.; Breyer, C. Techno-economic assessment of CO_2 direct air capture plants. *J. Clean. Prod.* **2019**, *224*, 957−980.
(29) Azarabadi, H.; Lackner, K. S. A sorbent-focused techno-economic analysis of direct air capture. *Appl. Energy* **2019**, *250*, 959−975.
(30) Young, J.; McQueen, N.; Charalambous, C.; Foteinis, S.; Hawrot, O.; Ojeda, M.; Pilorgé, H.; Andresen, J.; Psarras, P.; Renforth, P.; et al. The cost of direct air capture and storage can be reduced via strategic deployment but is unlikely to fall below stated cost targets. *One Earth* **2023**, *6*, 899−917.
(31) Deutz, S.; Bardow, A. Life-cycle assessment of an industrial direct air capture process based on temperature−vacuum swing adsorption. *Nat. Energy* **2021**, *6*, 203−213.
(32) Young, J.; Mcilwaine, F.; Smit, B.; Garcia, S.; van der Spek, M. Process-informed adsorbent design guidelines for direct air capture. *Chem. Eng. J.* **2023**, *456*, 141035.
(33) Anyanwu, J. T.; Wang, Y.; Yang, R. T. Amine-Grafted Silica Gels for CO_2 Capture including Direct Air Capture. *Ind. Eng. Chem. Res.* **2020**, *59*, 7072−7079.
(34) Darunte, L. A.; Sen, T.; Bhawanani, C.; Walton, K. S.; Sholl, D. S.; Realff, M. J.; Jones, C. W. Moving beyond Adsorption Capacity in Design of Adsorbents for CO_2 Capture from Ultradilute Feeds: Kinetics of CO_2 Adsorption in Materials with Stepped Isotherms. *Ind. Eng. Chem. Res.* **2019**, *58*, 366−377.
(35) Sakwa-Novak, M. A.; Yoo, C. J.; Tan, S.; Rashidi, F.; Jones, C. W. Poly(ethylenimine)-Functionalized Monolithic Alumina Honeycomb Adsorbents for CO_2 Capture from Air. *ChemSusChem* **2016**, *9*, 1859−1868.
(36) Grossmann, Q.; Stampi-Bombelli, V.; Yakimov, A.; Docherty, S.; Copéret, C.; Mazzotti, M. Developing Versatile Contactors for Direct Air Capture of CO_2 through Amine Grafting onto Alumina Pellets and Alumina Wash-Coated Monoliths. *Ind. Eng. Chem. Res.* **2023**, *62*, 13594−13611.
(37) Wang, Y.; Rim, G.; Song, M. G.; Holmes, H. E.; Jones, C. W.; Lively, R. P. Cold Temperature Direct Air CO_2 Capture with Amine-Loaded Metal-Organic Framework Monoliths. *ACS Appl. Mater. Interfaces* **2024**, *16*, 1404−1415.
(38) Tegeler, E.; Cui, Y.; Masoudi, M.; Bahmanpour, A. M.; Colbert, T.; Hensel, J.; Balakotaiah, V. A novel contactor for reducing the cost of direct air capture of CO_2. *Chem. Eng. Sci.* **2023**, *281*, 119107.
(39) Casas, N.; Schell, J.; Pini, R.; Mazzotti, M. Fixed bed adsorption of CO_2/H_2 mixtures on activated carbon: Experiments and modeling. *Adsorption* **2012**, *18*, 143−161.
(40) Ohs, B.; Krödel, M.; Wessling, M. Adsorption of carbon dioxide on solid amine-functionalized sorbents: A dual kinetic model. *Sep. Purif. Technol.* **2018**, *204*, 13−20.
(41) Bollini, P.; Brunelli, N. A.; Didas, S. A.; Jones, C. W. Dynamics of CO_2 adsorption on amine adsorbents. 1. impact of heat effects. *Ind. Eng. Chem. Res.* **2012**, *51*, 15145−15152.
(42) Bollini, P.; Brunelli, N. A.; Didas, S. A.; Jones, C. W. Dynamics of CO_2 adsorption on amine adsorbents. 2. insights into adsorbent design. *Ind. Eng. Chem. Res.* **2012**, *51*, 15153−15162.
(43) Kalyanaraman, J.; Fan, Y.; Lively, R. P.; Koros, W. J.; Jones, C. W.; Realff, M. J.; Kawajiri, Y. Modeling and experimental validation of carbon dioxide sorption on hollow fibers loaded with silica-supported poly(ethylenimine). *Chem. Eng. J.* **2015**, *259*, 737−751.
(44) Harlick, P. J.; Sayari, A. Applications of pore-expanded mesoporous silica. 5. triamine grafted material with exceptional CO_2 dynamic and equilibrium adsorption performance. *Ind. Eng. Chem. Res.* **2007**, *46*, 446−458.
(45) Bali, S.; Leisen, J.; Foo, G. S.; Sievers, C.; Jones, C. W. Aminosilanes grafted to basic alumina as CO_2 adsorbents-role of grafting conditions on CO_2 adsorption properties. *ChemSusChem* **2014**, *7*, 3145−3156.
(46) Garg, D. R.; Ruthven, D. M. Linear driving force approximations for diffusion controlled adsorption in molecular sieve columns. *AlChE J.* **1975**, *21*, 200−202.
(47) Farooq, S.; Ruthven, D. M. Heat Effects in Adsorption Column Dynamics. 1. Comparison of One- and Two-Dimensional Models. *Ind. Eng. Chem. Res.* **1990**, *29*, 1076−1084.
(48) Shafeeyan, M. S.; Wan Daud, W. M. A.; Shamiri, A. A review of mathematical modeling of fixed-bed columns for carbon dioxide adsorption. *Chem. Eng. Res. Des.* **2014**, *92*, 961−988.

https://doi.org/10.1021/acs.iecr.4c01392
Ind. Eng. Chem. Res. 2024, 63, 11637−11653

(49) Wilkins, N. S.; Rajendran, A.; Farooq, S. Dynamic column breakthrough experiments for measurement of adsorption equilibrium and kinetics. *Adsorption* **2021**, *27*, 397−422.
(50) Patton, A.; Crittenden, B. D.; Perera, S. P. Use of the linear driving force approximation to guide the design of monolithic adsorbents. *Chem. Eng. Res. Des.* **2004**, *82*, 999−1009.
(51) Perry, R. H.; Green, D. W.; Maloney, J. O. *Perry's Chemical Engineers' Handbook*, 7th ed.; McGraw-Hill Education: USA, 1999, pp 16−21.
(52) Glueckauf, E. Theory of chromatography. Part 10.- Formulæ for diffusion into spheres and their application to chromatography. *Trans. Faraday Soc.* **1955**, *51*, 1540−1551.
(53) John, D. fminsearchbnd. 2012. https://ch.mathworks.com/matlabcentral/fileexchange/8277-fminsearchbnd-fminsearchcon (accessed Mar 01, 2023).
(54) Wurzbacher, J. A.; Gebald, C.; Piatkowski, N.; Steinfeld, A. Concurrent Separation of CO_2 and H_2O from Air by a Temperature-Vacuum Swing Adsorption/Desorption Cycle. *Environ. Sci. Technol.* **2012**, *46*, 9191−9198.
(55) Yu, Q.; Brilman, D. W. Design Strategy for CO_2 Adsorption from Ambient Air Using a Supported Amine Based Sorbent in a Fixed Bed Reactor. *Energy Procedia* **2017**, *114*, 6102−6114.
(56) Knox, J. C.; Ebner, A. D.; Levan, M. D.; Coker, R. F.; Ritter, J. A. Limitations of Breakthrough Curve Analysis in Fixed-Bed Adsorption. *Ind. Eng. Chem. Res.* **2016**, *55*, 4734−4748.
(57) Gelles, T.; Rezaei, F. Diffusion kinetics of CO_2 in amine-impregnated MIL-101, alumina, and silica adsorbents. *AlChE J.* **2020**, *66*, 1−15.
(58) Wurzbacher, J. A.; Gebald, C.; Brunner, S.; Steinfeld, A. Heat and mass transfer of temperature-vacuum swing desorption for CO_2 capture from air. *Chem. Eng. J.* **2016**, *283*, 1329−1338.
(59) Climeworks, Orca: the first large-scale plant. 2021. https://climeworks.com/plant-orca (accessed Mar 21, 2024).
(60) Wiegner, J. F.; Grimm, A.; Weimann, L.; Gazzani, M. Optimal Design and Operation of Solid Sorbent Direct Air Capture Processes at Varying Ambient Conditions. *Ind. Eng. Chem. Res.* **2022**, *61*, 12649−12667.
(61) Elfving, J.; Sainio, T. Kinetic approach to modelling CO_2 adsorption from humid air using amine-functionalized resin: Equilibrium isotherms and column dynamics. *Chem. Eng. Sci.* **2021**, *246*, 116885.

https://doi.org/10.1021/acs.iecr.4c01392
Ind. Eng. Chem. Res. 2024, 63, 11637−11653